



# Electro-injection-enhanced catalytic formaldehyde degradation based on conductive $\text{MnO}_x$ cellulose aerogels at room temperature

De Cai Fang<sup>1</sup>, Jia Yu Zheng<sup>1</sup>, Chang Bao Han<sup>\*</sup>, Wen Kang Zhao, Yuan Gang Lu, Bei Chen Sun, Ling Sun, Xinxin Wang, Hui Yan

The Key Laboratory of Advanced Functional Materials, Ministry of Education of China, Faculty of Materials and Manufacturing, Beijing University of Technology, Beijing 100124, People's Republic of China

## ARTICLE INFO

### Keywords:

Manganese dioxide ( $\text{MnO}_x$ )  
Formaldehyde (HCHO)  
Conductive aerogel  
Catalytic oxidation  
Electron injection

## ABSTRACT

Transition metal oxide  $\text{MnO}_x$  shows great potential in catalytic formaldehyde (HCHO) pollution degradation at room temperature, but it is difficult to effectively overcome the catalyst deactivation caused by the accumulation of intermediates. Hereon, a 3D conductive aerogel catalyst with cellulose nanofibers (CNF) skeleton supported  $\text{MnO}_x$  nanoflowers and carbon black (CB) was prepared by freeze-drying. Based on the aerogel catalyst ( $\text{MnO}_x/\text{CB}/\text{CNF}$ ), an electro-injection-enhanced catalytic oxidation (EICO) strategy was proposed for HCHO degradation by promoting the formation lattice oxygen and reactive oxygen species  $\text{O}^*$ . In the dynamic test ( $\sim 15$  ppm at the weight hourly space velocity (WHSV) of  $600000 \text{ mL}/(\text{g}_{\text{MnO}_x}\cdot\text{h})$ ), the HCHO-to- $\text{CO}_2$  conversion efficiency of  $\text{MnO}_x/\text{CB}/\text{CNF}$  by electro-injection can be enhanced to 76.27%, which is 26.4% higher than that without electro-injection, and the corresponding dynamic efficiency did not show a decreasing trend within 72 h. This proposed EICO strategy may realize the efficient and long-term pollutant degradation at room temperature.

## 1. Introduction

With the continuous improvement of living conditions, more and more attention has been paid to indoor air pollution, and considering that people will spend about 80% of their life indoors, improving indoor air quality is crucial nowadays [1]. Indoor air pollution mainly comes from volatile organic compounds (VOCs) released by furniture, coatings and paints. Formaldehyde (HCHO), as a typical VOC, was listed as a Class 1 carcinogen by the International Agency for Research on Cancer (IARC) as early as 2004 [2], and long-term continuous exposure to it will greatly increase the risk of nose and throat cancer and leukemia [3]. Therefore, efficiently removing indoor HCHO is of great significance for improving indoor air quality and maintaining a healthy life. At present, the methods of removing indoor HCHO mainly include physical adsorption method [4], biological method [5], plasma method [6], photocatalytic method [7], room-temperature catalytic oxidation method [8] and more. Particularly, room-temperature catalytic oxidation is widely regarded as the most promising method [9] because of its high efficiency in removing HCHO and no toxic by-products in the catalytic process, it can be directly used in the indoor environment. The

catalysts used at room temperature for HCHO removal could be divided into noble metal catalysts and non-noble metal catalysts. Noble metal catalysts, such as Pt, Ru, Pd, etc., have an efficient capacity for HCHO catalytic oxidation, but their practical application is seriously limited due to the high price and low abundance [10–12]. Therefore, some non-noble metal catalysts have been paid more and more attention due to their excellent HCHO removal efficiency and low price [13–15].

Among the non-noble metal catalysts, manganese oxide ( $\text{MnO}_x$ ) has been widely studied due to its excellent room-temperature catalytic activity, high abundance and non-toxicity [16–18]. In 2020, Ji et al. [19] reported that a potassium-modulated  $\delta\text{-MnO}_2$  achieves efficient degradation ( $\sim 100\%$  HCHO removal efficiency and  $\sim 40\%$   $\text{CO}_2$  production efficiency) of 22 ppm HCHO at  $30^\circ\text{C}$  under a weight hourly space velocity (WHSV) of  $200,000 \text{ mL}/(\text{g}_{\text{cat}}\cdot\text{h})$ . Nevertheless, the long-term stability of the  $\text{MnO}_x$  catalyst used indoors is not ideal according to previous studies. For instance, Li et al. [20] found that the continuous catalytic efficiency of  $\text{MnO}_x/\text{active carbon}$  catalyst decreased sharply at 5 h for HCHO with a concentration of 4 ppm. Since intermediates (such as methane acid, formate species, etc.) produced during the catalytic process could not be decomposed on time, which

<sup>\*</sup> Corresponding author.

E-mail address: [cbhan@bjut.edu.cn](mailto:cbhan@bjut.edu.cn) (C.B. Han).

<sup>1</sup> The authors contribute equally to the article

would cover the surface-active sites of the catalyst and result in the deactivation of catalysis. Theoretical research reveals that the generation capacity of reactive oxygen species  $O^*$  ( $O$ ,  $O_2$ ,  $O_2^-$ , etc.) is determined by the migration of lattice oxygen ( $O_{latt}$ ) in  $MnO_x$  (i.e., the valence transformation of Mn), which is the key to oxidizing and decomposing intermediates [21]. Therefore, numerous works enhance the production of  $O^*$  by promoting the  $O_{latt}$  migration in  $MnO_x$  to improve room-temperature catalytic activity and long-term stability of catalysts [22,23].

Zou et al. [24] first proposed a scheme to improve the stability of the  $MnO_x$  catalyst by joule heating (138 °C), and the HCHO removal efficiency was persistently maintained at around 90% in the 8-times cycle test. This is attributed to the accelerated migration of  $O_{latt}$  in  $MnO_x$  with the assistance of joule heating, which generates a large amount of  $O^*$  and makes the catalyst exhibit excellent stability by decomposing intermediates. However, the catalyst with high-temperature reactions will inevitably cause safety risks that cannot be ignored when used indoors, thus limiting its further development and practical application. In addition, Zhao et al. [25] prepared a self-driven triboelectric catalyst ( $MnO_x$ -PMMA-SSM), which shows higher HCHO-to- $CO_2$  conversion efficiency (36.25%) than that of the traditional  $MnO_x$  catalyst, owing excellent catalytic activity at room temperature. The triboelectric charge generated by  $MnO_x$ -PMMA-SSM under wind drive enhances the transition of O atoms between  $O_2$ ,  $O_{latt}$  and  $O^*$  species, promoting the oxidation decomposition of intermediates and the conversion of HCHO to  $CO_2$ . Even so, this method relies too much on the constant existence of mechanical energy indoors, and the electron quantity generated is volatile, which may lead to the unstable efficiency of the catalyst. Therefore, exploring a safe and stable method to enhance the production of  $O^*$  is unprecedentedly critical to improving the efficiency and stability of HCHO degradation by  $MnO_x$  catalyst at room temperature. Interestingly, Mei et al. [26] reported an electrification strategy to reduce the soot ignition temperature by applying an electric current to a conductive oxide catalyst (K/ATO) to promote the migration and release of lattice oxygen, the soot ignition temperature is reduced by nearly 4 times compared with the not electrified. It is reasonable to be speculated that direct injection of electrons into the catalyst with the assistance of a stable and controlled external electric field could induce the migration of  $O_{latt}$  inside  $MnO_x$  to promote the generation of  $O^*$ , which may be an optimization strategy to simultaneously increase catalyst activity and stability at room temperature.

Furthermore,  $MnO_x$  catalysts usually exist in the form of powder, which will not only cause waste of active sites due to agglomeration but also dust pollution in the process of practical application [27,28]. Thus, it is critical to select a material with a large specific surface area and high porosity as the carrier for  $MnO_x$  to solve the above problems in realistic application [29]. Aerogels are widely used as the carrier material for various catalysts due to their unique characteristics of low density, high surface area and ultra-high porosity [30]. Based on a three-dimensional (3D) aerogel skeleton with high surface area and porosity, the active sites of  $MnO_x$  can be better exposed, at the same time, the reciprocal flow and adsorption-desorption of gas molecules during the process of catalysis could be promoted greatly. Moreover, considering that the mode of electron injection by an external electric field has higher requirements for the conductivity of the material, it may be a feasible strategy to prepare conductive aerogel composite catalysts loaded with  $MnO_x$  on the premise of ensuring the inherent structure of aerogel.

In this work, the physical-chemical bonds co-cross-linked 3D conductive aerogels were prepared by the freeze-drying method based on the chemical bond between cellulose nanofiber (CNF) and epichlorohydrin (ECH), hydrogen bonds among  $MnO_x$ , carbon black (CB) and CNF. This aerogel catalyst ( $MnO_x$ /CB/CNF) not only owns the characteristics of low density, high specific surface area and high porosity, but also shows superior electrical conductivity. For improving the catalytic-oxidative capacity of HCHO, an electro-injection-enhanced catalytic oxidation (EICO) strategy was proposed based on the conductive aerogel

catalyst  $MnO_x$ /CB/CNF. The static HCHO removal efficiency, dynamic HCHO removal efficiency, dynamic HCHO-to- $CO_2$  conversion efficiency and long-term stability were tested in this work. The promotion mechanism under the condition of electron injection was clarified according to the electrical properties of the catalyst. This study innovatively proposed and discussed the catalytic oxidation behavior of the  $MnO_x$  catalyst under the action of electron injection, which is expected to solve the long-term catalytic problem of formaldehyde at room temperature.

## 2. Experimental

### 2.1. Material synthesis

#### 2.1.1. Chemicals

All reagents are analytical grade and used directly after purchase without further purification, including potassium permanganate ( $KMnO_4$ ), ammonium oxalate ( $(NH_4)_2C_2O_4$ ) and epichlorohydrin (ECH). Commercial cellulose nanofibers aqueous solution (1.0 wt%) was purchased from Qihong Technology Co., Ltd. (Guilin) with a diameter of 4–10 nm and a length of 1–3  $\mu m$ . Conductive carbon black was purchased from CABOT company in the United States.

#### 2.1.2. Synthesis of $MnO_x$ powder

Firstly, 0.79 g  $KMnO_4$  and 1.1169 g  $(NH_4)_2C_2O_4$  were dissolved in 100 mL and 30 mL deionized water respectively, after stirring vigorously for 2 h, the two solutions were mixed and stirred again for 1 h to get a uniform mix solution. After adjusting the pH value of the mixed solution to 7.3, it was placed in the reaction kettle and reacted at 90 °C for 10 h to obtain black mud. The obtained black mud was repeatedly cleaned and filtered with deionized water 4 times, and then placed in a tubular furnace at 105 °C for 12 h to obtain brown  $MnO_x$  nanoparticles finally.

#### 2.1.3. Synthesis of the $MnO_x$ /CB/CNF aerogel

In the beginning, 12.5 mL CNF colloids with a mass fraction of 1.0 wt% were dissolved in 12.5 mL deionized water, then the mixed solution was crushed in an ultrasonic cell crusher with 30% power for 20 min to obtain CNF dispersion with the mass fraction of 0.5 wt%. Subsequently, 0.6 g  $MnO_x$  powder and 0.5 mL ECH were added to the CNF dispersion solution (0.5 wt%), continuously stirring for 4 h to make them fully dispersed. Next, the CB with different masses (0 g, 0.08 g, 0.18 g, 0.310 g, 0.483 g) was added to the above-mixed solution. After stirring for 4 h pour the mixture into three 3.5 cm diameter cylindrical molds, rapidly frozen with liquid nitrogen for 20 min, and then placed in a freeze dryer (DTY-8 L, China) for 48 h to obtain  $MnO_x$ /CB(<sub>n</sub>)/CNF aerogel, where “n” represents the mass fraction of CB in the whole aerogel (0 wt%, 10 wt%, 20 wt%, 30 wt%, 40 wt%), namely  $MnO_x$ /CB(0, 0.1, 0.2, 0.3, 0.4)/CNF.

### 2.2. Characterizations

The morphologies of the samples were studied by field emission scanning transmission electron microscopy (FE-STEM, SU9000, Japan), and the distributions of Mn, C, and O elements were obtained by energy dispersive X-ray spectroscopy (EDX, EDAX, USA) mapping. The microstructure of the sample was observed by a field emission transmission electron microscope (TEM, FEI Talos F200X, USA) at an accelerating voltage of 200 kV. The specific surface areas and pore size distribution were examined based on the Brunauer-Emmett-Teller (BET) and Barrett-Joyner-Halenda (BJH) methods, respectively (Micromeritics ASAP 2460, USA). The phase structure of different samples was determined by X-ray diffractometer (XRD, Bruker D8, Germany) with  $Cu K_{\alpha 1}$  radiation ( $\lambda = 1.5406 \text{ \AA}$ ), and Raman spectra of the samples were excited by Raman spectroscopy (RENISHAW InVia Reflex, U.K.) using a laser light source with a wavelength of 532 nm. To analyze the surface chemical state of the catalyst, it was characterized by X-ray photoelectron spectroscopy (XPS, Thermo-ESCALAB 250XI, USA). Use a thermal imager (FOTRIC 326 C, USA) to monitor the temperature change of the sample

when energized. The changes of the surface groups during the removal of HCHO from the catalysts were monitored by in-situ infrared spectroscopy (In-situ DRIFTS, Thermo-Nicolet iS10, USA) in the wave-number range of 1000–4000  $\text{cm}^{-1}$ . The surface free radicals of the samples were measured by electron paramagnetic resonance (EPR, Bruker EMX PLUS, Germany) at room temperature.

### 2.3. Evaluation tests of the sample for HCHO catalytic degradation

The catalytic activity and stability of the samples were evaluated by static and dynamic tests at room temperature. The EICO static test device is mainly composed of a 48000 mL polymethyl methacrylate glove box, circulation system, power supply system and monitoring system (Fig. S1). Typically, two pieces of aerogel samples ( $2 \times 9.62 \text{ cm}^2$ ) are placed in a tube with a fan, with mesh copper electrodes attached to both ends of the sample and connected to a DC power supply, and the entire tube is placed in a sealed bag in the test chamber. Then 8  $\mu\text{L}$  of HCHO (38 wt%) solution was injected into the test chamber, and the test chamber was closed. The sealed bag was opened and the power supply connected to the sample was switched on to test the HCHO catalytic activity of the sample when the indicator of the HCHO tester (PPT-HTV, UK, the measuring range is 0–20 ppm, the test accuracy is 0.01 ppm) is stable. Furthermore, the EICO dynamic tests and stability tests of HCHO removal were also performed in this work. In dynamic tests (Fig. S2), a piece of aerogel sample ( $1 \times 9.62 \text{ cm}^2$ ,  $C_{\text{MnO}_x} \sim 0.2 \text{ g}$ ) was placed in the reaction tube (40 mL), and copper mesh electrodes were affixed to both sides of the aerogel. The copper mesh electrodes were connected to the DC power supply, and the HCHO gas (RH: 45%,  $\text{O}_2$ : 21 Vol%, HCHO initial concentration:  $\sim 15 \text{ ppm}$ , the rest is  $\text{N}_2$ ) continuously through the sample with a constant flow rate of 2000 mL/min corresponded to a weight hourly space velocity (WHSV) of 600000  $\text{mL/g}_{\text{MnO}_x}\cdot\text{h}$ , and the gas at the outlet is monitored by the HCHO and  $\text{CO}_2$  testers in real-time. Particularly, the electrical properties of samples are tested,  $\text{MnO}_x$  and  $\text{MnO}_x/\text{CB}/\text{CNF}$  with different CB contents were pressed into  $1 \times 1 \text{ cm}$  slices with a thickness of 0.1 mm and placed in a special device to test the I-V curve (Fig. S6a), applying a voltage of 10 V to the sample. In addition,  $\text{CO}_2$  products were measured with a photoacoustic field gas monitor (INNOVA Air Tech Instruments, China, the measuring range is 0–100 ppm, the test accuracy is 0.1 ppm) to calculate HCHO-to- $\text{CO}_2$  conversion efficiency for evaluating the oxidative degradation ability of catalysts in HCHO removal. The control group was set to avoid the influence of temperature rise caused by electron injection in the efficiency tests: the copper grid electrode was replaced by an electrically heated porous ceramic plate, and the temperature of the ceramic plate was controlled by different voltages to compare with the energized sample. In static test, HCHO removal efficiency is calculated by the below formula:

$$\text{HCHO removal efficiency} = \frac{C_{\text{HCHO}} - \text{initial} - C_{\text{HCHO}} - \text{final}}{C_{\text{HCHO}} - \text{initial}} \times 100\% \quad (1)$$

In the Eq. (1),  $C_{\text{HCHO}} - \text{initial}$  and  $C_{\text{HCHO}} - \text{final}$  respectively corresponds to the initial concentration of HCHO the final HCHO concentration at the end of the catalytic reaction in the static test tank, and the units of all unknown variables are ppm.

In dynamic test, HCHO removal efficiency and HCHO-to- $\text{CO}_2$  conversion efficiency are calculated by the below formulas:

$$\text{HCHO removal efficiency} = \frac{C_{\text{HCHO}} - \text{inlet} - C_{\text{HCHO}} - \text{outlet}}{C_{\text{HCHO}} - \text{inlet}} \times 100\% \quad (2)$$

$$\text{HCHO-to-}\text{CO}_2 \text{ conversion efficiency} = \frac{C_{\text{CO}_2} - \text{outlet}}{C_{\text{HCHO}} - \text{inlet}} \times 100\% \quad (3)$$

In the above Eqs. (2) and (3),  $C_{\text{HCHO}} - \text{inlet}$ ,  $C_{\text{HCHO}} - \text{outlet}$  and  $C_{\text{CO}_2} - \text{outlet}$  correspond to the HCHO concentrations in the inlet and HCHO concentrations in the outlet gases and  $\text{CO}_2$  concentrations in the outlet gases respectively. And the units of all unknown variables are ppm.

## 3. Results and discussion

### 3.1. Synthesis, morphology and phase structures

Based on the freeze-drying method, different samples of CNF,  $\text{MnO}_x/\text{CNF}$  and  $\text{MnO}_x/\text{CB}/\text{CNF}$  aerogels were prepared in this work, and the schematic diagrams of the above samples were shown in Fig. 1a. Particularly, the construction mechanism of  $\text{MnO}_x/\text{CNF}$  aerogel is as follows (Fig. 1b): firstly, the hydrogen bonds between CNF are destroyed by an ultrasonic crusher to obtain small cellulose fragments; and then  $\text{MnO}_x$  particles with the structure of nanoflowers are anchored on the cellulose skeleton by hydrogen bonding force; in the meantime, the other cellulose fragments are intercoupled with themselves by forming ethers chemical bonds with ECH to realize the construction of aerogel with network structure [31,32]. Further, the conductive aerogel  $\text{MnO}_x/\text{CB}/\text{CNF}$  was prepared by introducing CB on the basis of  $\text{MnO}_x/\text{CNF}$  aerogel, which owns so extremely light weight that could be easily supported by the stamens of a flower as shown in Fig. 1c.

In the photos of Fig. 2a1, b1 and c1, all of the prepared aerogel samples show 3D-blocky structures. A number of reticular macroporous with a diameter ranging from 1 to 5  $\mu\text{m}$  could be observed in the SEM images of pure CNF aerogel, and the porous structure was constructed by the polymerization and interconnection of CNF during freeze-drying (Fig. 2a2-a4) [33]. In the SEM images of  $\text{MnO}_x/\text{CNF}$  (Fig. 2b2-b4),  $\text{MnO}_x$  powders split the initial large pores in CNF aerogel into a larger number of smaller nanopores in the manner of in-situ self-supported growth. Moreover, considering CB particles own good electrical conductivity and small size that is easy to disperse, the conductive aerogel  $\text{MnO}_x/\text{CB}/\text{CNF}$  was obtained by introducing CB into  $\text{MnO}_x/\text{CNF}$ . In Fig. S3a-d, the pore structure of the aerogel samples began to collapse with the continuous introduction of CB, and the macroporous disappeared when the doping amount of CB exceeded 0.2 wt% particularly. Thus, in order to comprehensively balance the conductivity and structural integrity of the material, the  $\text{MnO}_x/\text{CB}/\text{CNF}$  aerogel with 0.2 wt% CB ( $\text{MnO}_x/\text{CB}_{0.2}/\text{CNF}$ ) was used as the target sample for subsequent studies, and the SEM images of which were shown in Fig. 2c2-c4. Combining with the EDX mapping images (Fig. S3e-h), it can be seen that CB (C element) and  $\text{MnO}_x$  (Mn element) particles successfully implemented staggered and uniform dispersion on the basis of maintaining the original porous structure of CNF aerogel in  $\text{MnO}_x/\text{CB}_{0.2}/\text{CNF}$ . This combination mode of CB,  $\text{MnO}_x$  and CNF aerogel could optimize the contact mode of  $\text{MnO}_x$  particles with itself or CB, which is conducive to directly or indirectly injecting electrons into  $\text{MnO}_x$  in the subsequent catalysis with the assistance of electron injection.

In TEM characterization (Fig. 2d-f), it is found that  $\text{MnO}_x$ , CB and CNF as the three parts of  $\text{MnO}_x/\text{CB}/\text{CNF}$  aerogel achieved stable combined reconstruction, and  $\text{MnO}_x$  component exhibits a flower-like structure that is consistent with the SEM images. Moreover, the lattice fringes with the interval of 0.272 nm, 0.309 nm and 0.246 nm were observed in the high-resolution lattice diffraction patterns (Fig. 2f), which corresponds to the (222), (310) and (021) crystal planes of  $\text{Mn}_2\text{O}_3$ ,  $\text{MnO}_2$  and  $\text{MnO}$  respectively [34–36]. Therefore, it can be inferred that  $\text{MnO}_x$  in  $\text{MnO}_x/\text{CB}_{0.2}/\text{CNF}$  aerogel is a multiphase composite oxide with mixed valence. In the process of HCHO catalytic oxidation by the conductive aerogel catalyst  $\text{MnO}_x/\text{CB}/\text{CNF}$  under the action of EICO strategy, the catalyst was defined to  $\text{MnO}_x/\text{CB}/\text{CNF}$  with electro-injection ( $\text{MnO}_x/\text{CB}/\text{CNF-EI}$ ). In particular, the components of  $\text{MnO}_x$ , CB, CNF and IE as controllable variables in catalysis, which play different roles in HCHO removal process: (1)  $\text{MnO}_x$  as the catalytic active substance, which catalyzes  $\text{O}_2$  and  $\text{H}_2\text{O}$  in the air to generate



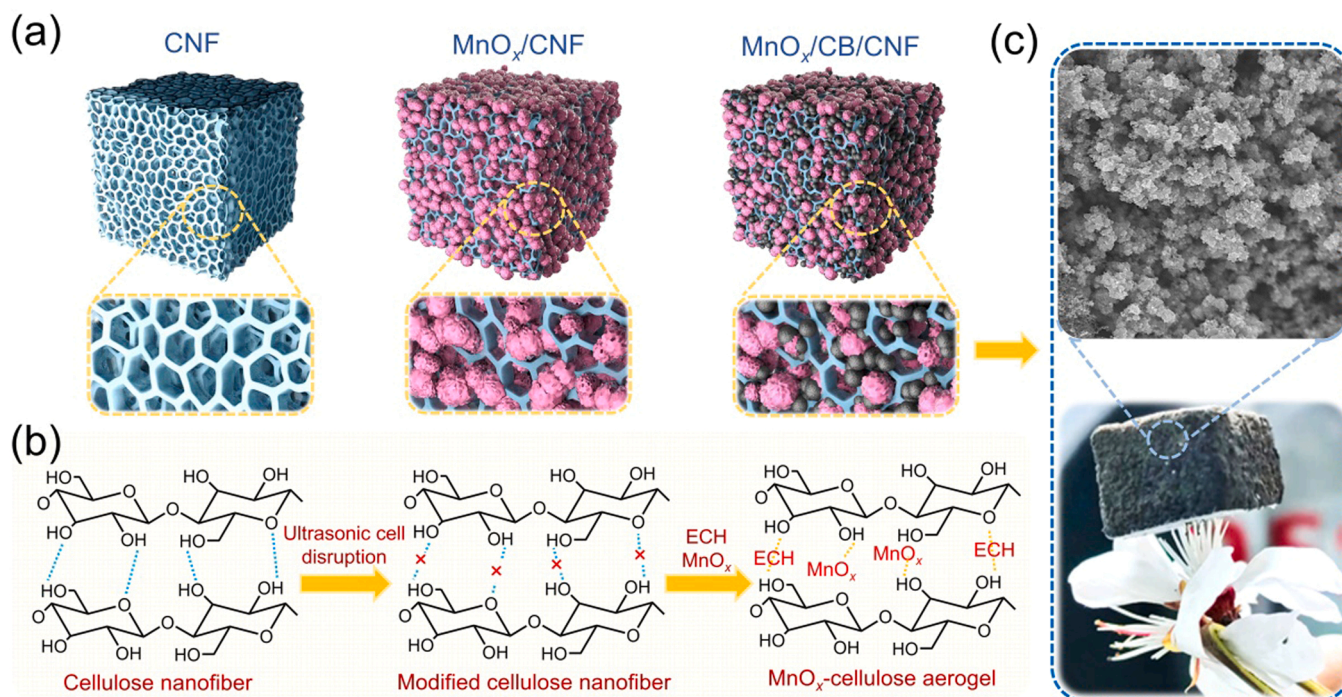


**Fig. 1.** (a) Schematic diagram of the structure of different aerogel samples: CNF, MnO<sub>x</sub>/CNF and MnO<sub>x</sub>/CB/CNF. (b) The formation mechanism diagram of the chemical bonds in MnO<sub>x</sub>/CNF aerogel. (c) The photograph and SEM image of aerogel catalyst MnO<sub>x</sub>/CNF.

reactive oxygen species with strong oxidation to oxidative HCHO degradation; (2) CB as the nano-conductive agent, it can increase the overall conductivity of the catalyst and provide a basic condition for constructing the electro-injection enhanced catalyst; (3) CNF as the organic skeleton, it is responsible for fixing nano-sized MnO<sub>x</sub> and CB particles synchronously and constructing the 3D porous aerogel materials with low wind resistance; (4) EI is the electron injection technology via an external power supply, which also is key element of the ECIO strategy.

The crystal structure of MnO<sub>x</sub> catalyst and different aerogel samples were studied by XRD tests as shown in Fig. 3a. The pure CNF aerogel has no XRD characteristic peaks detected, which shows a typical amorphous structure. The characteristic diffraction peaks of MnO<sub>x</sub> located at 12.3°, 25.2°, 36.8°, and 66.3°, respectively corresponding to the crystal planes (001), (002), (−111), (020) of δ-MnO<sub>2</sub> (JCPDS 80–1098) [24,37–39]. Obvious characteristic peaks of MnO<sub>2</sub> are found in the XRD pattern of MnO<sub>x</sub>/CNF aerogel, which can be inferred that the Mn-based catalytic active materials have been successfully introduced into the base material of CNF aerogel. In addition, the XRD diffraction peaks intensity of MnO<sub>x</sub>/CB/CNF aerogel does not change significantly with the increase of CB content, indicating that the phase structure of MnO<sub>x</sub> will not be changed by the modification of CB. Moreover, in the Raman spectra of different MnO<sub>x</sub>/CB/CNF aerogel samples (Fig. 3b), the characteristic peaks of D and G bands corresponding to carbon material are enhanced with the increased content of CB particles [40,41], meaning which were successfully doped into the catalytic aerogel sample MnO<sub>x</sub>/CB/CNF. In addition, the phase structure of MnO<sub>x</sub>/CB<sub>0.2</sub>/CNF aerogel with electro-injection (MnO<sub>x</sub>/CB<sub>0.2</sub>/CNF-EI) was compared with that of MnO<sub>x</sub>/CB<sub>0.2</sub>/CNF without electron injection in the Raman spectra as shown in Fig. 3b. The characteristic peak of Mn–O was weakened when the sample MnO<sub>x</sub>/CB<sub>0.2</sub>/CNF was energized for 10 min, it is speculated that the electron density around Mn is changed by the injection of electrons, leading to part of the lattice oxygen (O<sub>latt</sub>) escape from MnO<sub>x</sub> lattice [42].

The surface chemical state analysis of MnO<sub>x</sub>/CB<sub>0.2</sub>/CNF aerogel with and without electron injection was characterized by the XPS tests (Fig. 3c–e, Fig. S4). Mn 2p spectrum is shown in Fig. 3c, it can be found

that the peak area of Mn<sup>3+</sup> (642.0 eV) increases but Mn<sup>4+</sup> (643.2 eV) decreases after MnO<sub>x</sub>/CB<sub>0.2</sub>/CNF being processed by electron injection. In the XPS spectrum of O 1s (Fig. 3d), there are three peaks at 529.5 eV, 531.5 eV and 532.9 eV, corresponding to lattice oxygen (O<sub>latt</sub>), oxygen vacancy/surface hydroxyl group (O<sub>v</sub>/O<sub>H</sub>) and surface adsorbed oxygen (O<sub>A</sub>), respectively [43]. Combining with the Mn 2p spectrum, the increase of O<sub>v</sub>/O<sub>H</sub> after the sample was electrified further confirms that the O<sub>latt</sub> species of MnO<sub>x</sub>/CB<sub>0.2</sub>/CNF would escape and form oxygen vacancies under the action of electron injection [44,45]. The element content of the sample with and without electron injection are shown in Fig. 3f, about 16% Mn<sup>4+</sup> converts to Mn<sup>3+</sup> and 8% O<sub>v</sub> is generated after the sample was electrified, and more than 10% O<sub>A</sub> disappears due to it gaining electrons to become reactive oxygen species O\* under the action of electron injection. The above information reveals that the assistance of electron injection to the catalyst could accelerate the migration of O<sub>latt</sub> by inducing the redistribution of electron density and the rapid migration of electrons, and then enhance the generation of O\* species for HCHO oxidation. In addition, the characteristic peaks of C 1s are deconvoluted into three peaks located at 284.6, 286.1 and 288.1 eV corresponding to C=C, C–O and C=O, respectively [46], further confirming the existence of CNF and CB CNF and CB containing carbon element in MnO<sub>x</sub>/CB<sub>0.2</sub>/CNF aerogel.

The specific surface area and pore structure of MnO<sub>x</sub>/CB<sub>0.2</sub>/CNF and MnO<sub>x</sub>/CNF aerogel were characterized by BET tests as shown in Fig. 3g–h. The adsorption models of both two samples are type IV isothermal adsorption and desorption curves, and the hysteresis loop is type h3 (Fig. 3g), indicating that the aerogel catalyst has more slit-type pores inside [47]. It can be seen that the pores of MnO<sub>x</sub>/CNF are mostly large, while the pores of MnO<sub>x</sub>/CB<sub>0.2</sub>/CNF are mainly mesopores of 3–5 nm according to the aperture distribution curve in Fig. 3h [48], meaning that MnO<sub>x</sub>/CB<sub>0.2</sub>/CNF may exhibit a larger specific surface area to capture the target gas on its active sites during catalysis. In order to evaluate the comprehensive characteristics of the porous aerogels, the radar plots of density, specific surface area, porosity and electrical conductivity of different aerogel samples are summarized in Fig. 3i. In particular, MnO<sub>x</sub>/CB<sub>0.2</sub>/CNF shows a higher surface area than MnO<sub>x</sub>/CNF (the surface area of MnO<sub>x</sub>/CNF is 90.043 m<sup>2</sup>/g, the surface



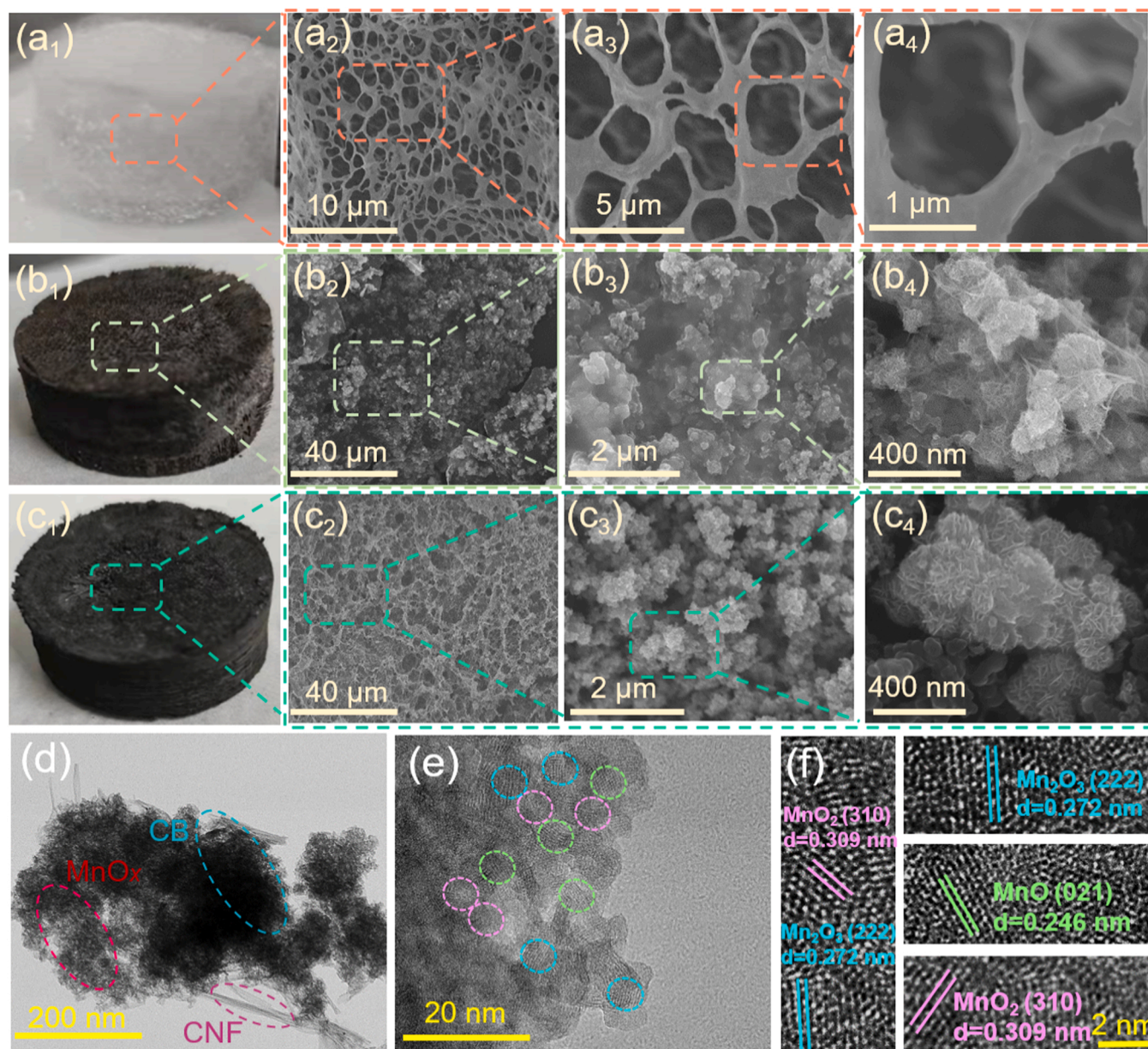


**Fig. 2.** The photos and SEM images of (a1-a4) CNF aerogel, (b1-b4)  $\text{MnO}_x/\text{CNF}$  aerogel and (c1-c4)  $\text{MnO}_x/\text{CB}_{0.2}/\text{CNF}$  aerogel. (d-f) TEM images of  $\text{MnO}_x/\text{CB}_{0.2}/\text{CNF}$  aerogel at different magnifications.

area of  $\text{MnO}_x/\text{CB}_{0.2}/\text{CNF}$  is  $105.20 \text{ m}^2/\text{g}$ ), which may be attributed to that the modest addition of CB nanoparticles promotes the process of large pores splitting into smaller ones on the basis of maintaining the structure of the cellulose aerogel, and this inference is consistent with the results of SEM images. Consequently, to balance the effect of CB on the conductivity and the specific surface area of the aerogel catalyst,  $\text{MnO}_x/\text{CB}_{0.2}/\text{CNF}$  with 0.2 wt% CB was selected as the optimal catalytic aerogel for the subsequent study due to the small density ( $< 40 \text{ mg}/\text{cm}^3$ ), well electrical conductivity ( $\sim 2.11 \text{ S}/\text{m}$ ) and very high porosity ( $> 87\%$ ) of it.

### 3.2. Activity for HCHO degradation

Firstly, the HCHO catalytic degradation ability of different samples with and without electron injection was evaluated. The EICO static test chamber and its interior structure are shown in Fig. S1. Particularly, electron injection was performed into the catalyst during the catalytic process as shown in Fig. 4a. As shown in Fig. 4b, the HCHO removal

efficiency of  $\text{CB}_{0.2}/\text{CNF}$  with electron injection ( $\text{CB}_{0.2}/\text{CNF-EI}$ ) has no obvious increase than  $\text{CB}_{0.2}/\text{CNF}$  without electron injection, which indicated that electron injection has no effect on HCHO removal capacity for the aerogel sample that in the absence of the catalyst. However, the HCHO removal efficiency of  $\text{MnO}_x/\text{CB}/\text{CNF}$  was significantly improved when it was injected with electrons. Particularly,  $\text{MnO}_x/\text{CB}_{0.2}/\text{CNF}$  shows the best removal efficiency among all samples, and it could reduce the HCHO from 9.87 ppm to 0.056 ppm (below the standard limit value of 0.08 ppm) within 90 min with the assistance of electron injection (Fig. 4c and d). Besides,  $\text{MnO}_x/\text{CB}_{0.2}/\text{CNF}$  also shows the most significant increase in catalytic activity among all catalytic aerogel samples, and the efficiency of which increased from 88.46% to 99.42% in the static tests and from 89.78% to 99.21% in the dynamic tests (Fig. 4e).

In order to further explore the catalytic enhancement effect by electron injection on HCHO removal, the production of final product  $\text{CO}_2$  and the efficiency of HCHO-to- $\text{CO}_2$  conversion efficiency by the samples of  $\text{MnO}_x/\text{CNF}$  and  $\text{MnO}_x/\text{CB}_{0.2}/\text{CNF}$  with or without electron

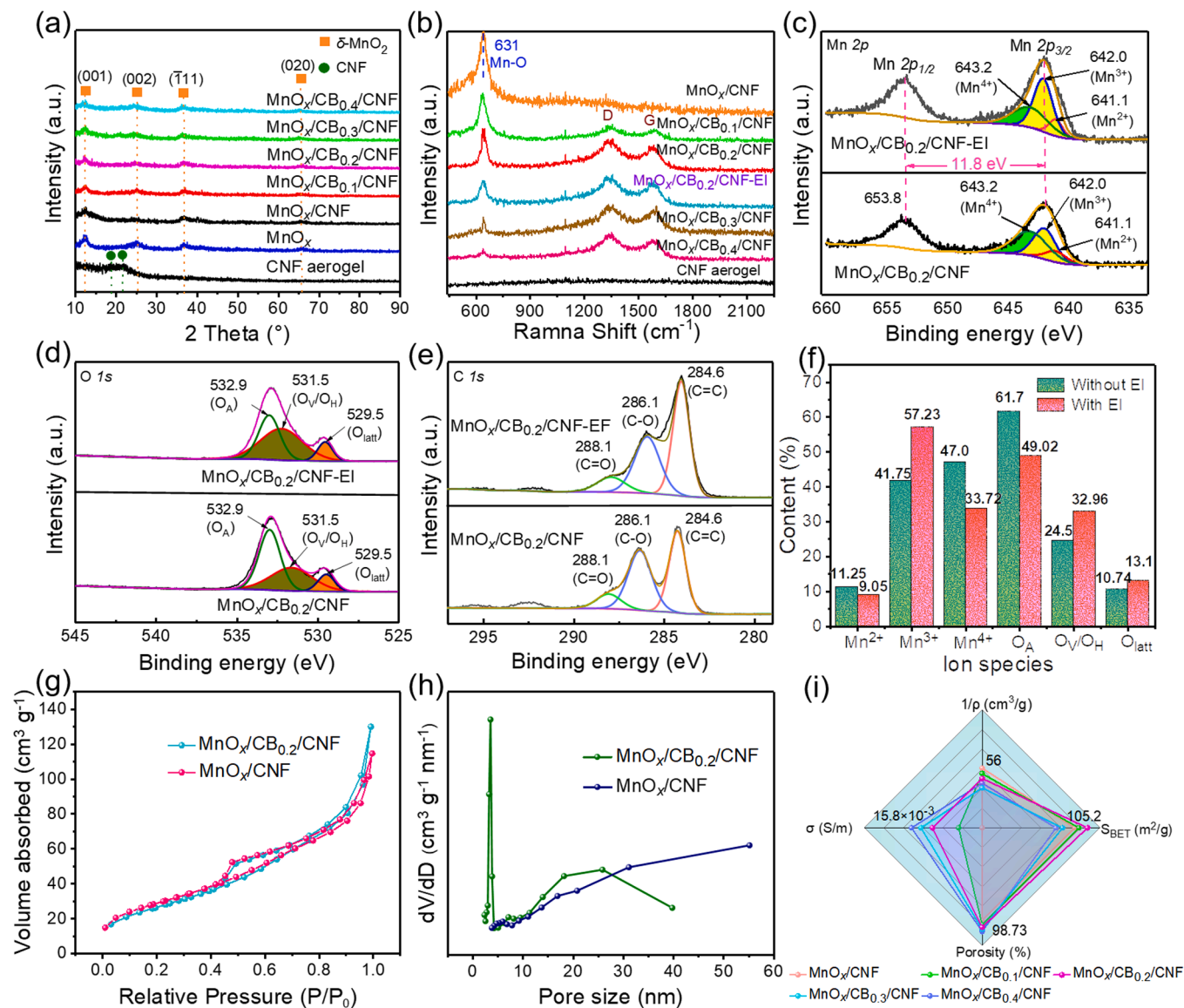


**Fig. 3.** (a) XRD patterns and (b) Raman spectra of CNF, MnO<sub>x</sub>, MnO<sub>x</sub>/CNF and MnO<sub>x</sub>/CB/CNF with different CB contents. (c-e) XPS spectra of MnO<sub>x</sub>/CB<sub>0.2</sub>/CNF that with and without electron injection: (c) Mn 2p, (d) O 1s, (e) C 1s. (f) Bar chart of changes in Mn valence and O species percentage of MnO<sub>x</sub>/CB<sub>0.2</sub>/CNF that with and without electron injection. (g) N<sub>2</sub> adsorption-desorption isotherm curve and (h) pore size distribution curve of MnO<sub>x</sub>/CB<sub>0.2</sub>/CNF. (i) Radar plot of surface area, the inverse of density, porosity and electrical conductivity of CNF, MnO<sub>x</sub>/CNF and MnO<sub>x</sub>/CB/CNF with different CB contents.

injection were evaluated by the EICO dynamic device shown in Fig. S2. It was found that CO<sub>2</sub> production increases significantly (up to 11.44 ppm) when MnO<sub>x</sub>/CB<sub>0.2</sub>/CNF was energized (Fig. 4f), and the HCHO-to-CO<sub>2</sub> conversion efficiency of which with electron injection increase by 27.4% and 24.67% compared with MnO<sub>x</sub>/CNF and MnO<sub>x</sub>/CB<sub>0.2</sub>/CNF respectively (Fig. 4g). It is indicated that electron injection has a significant improvement for HCHO convert to final product CO<sub>2</sub> during the catalysis at room temperature. In addition, the long-term stability of aerogel catalysts was evaluated by dynamic and static life-times tests. In the dynamic life test within 72 h, it was found that the dynamic removal HCHO efficiency of MnO<sub>x</sub>/CB<sub>0.2</sub>/CNF was maintained at a high level all the time when the sample with electron injection, while the dynamic efficiency of MnO<sub>x</sub>/CB<sub>0.2</sub>/CNF without electron injection decreased significantly (Fig. 4 h). Moreover, in the static life test, two pieces of MnO<sub>x</sub>/CB<sub>0.2</sub>/CNF (0.4 g) with electron injection were put into the EICO static test chamber for cyclic HCHO removal ability tests. After six cycle tests, the HCHO removal efficiency of MnO<sub>x</sub>/CB<sub>0.2</sub>/CNF basically did not decay (Fig. 4i), meaning the sample own excellent catalytic stability of HCHO removal.

### 3.3. Mechanism of HCHO catalytic oxidative degradation with electron injection

During the catalysis of the aerogel samples with electron injection, the temperature change of which was monitored by an infrared camera as shown in Fig. 5a-b. When the input voltage is controlled in the range of 0–30 V, the temperature of MnO<sub>x</sub>/CB<sub>0.2</sub>/CNF increases with the increase of the voltage (Fig. S5a-h). Especially in the range of 0–15 V, the temperature of the sample is lower than 25 °C, which belongs to the category of room temperature. Therefore, in order to investigate the effect of electron injection on HCHO degradation by aerogel catalysts at room temperature, the efficiency of HCHO removal was tested at the voltage of 0–15 V (Fig. S5i). The result shows that HCHO removal efficiency of MnO<sub>x</sub>/CB<sub>0.2</sub>/CNF increases with the increase of voltage, and the efficiency with the voltage of 10 V is similar to that of 15 V. Hereon, synchronously considering the energy saving and the temperature change of the catalyst, all of the subsequent catalytic efficiency tests were carried out under the voltage of 10 V. Fig. 5c shows the temperature variation of MnO<sub>x</sub>/CB/CNF with different CB content at 10 V DC



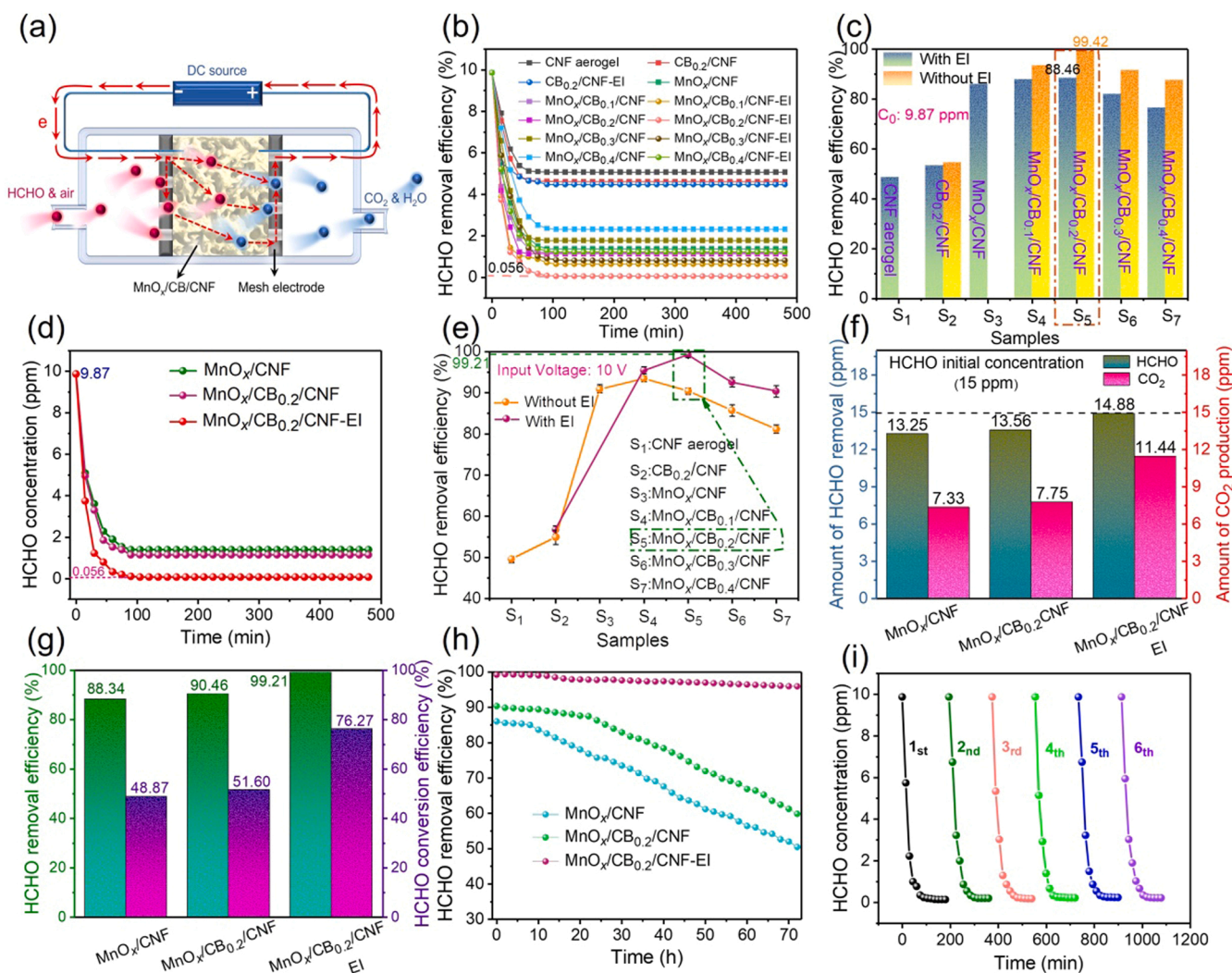


**Fig. 4.** (a) The diagram of aerogel catalyst with electron injection. (b-c) Static efficiency tests of CNF, MnO<sub>x</sub>, MnO<sub>x</sub>/CNF and MnO<sub>x</sub>/CB/CNF with different CB contents were statically tested under energization or non-energization conditions (Temperature: ~25 °C; voltage: 10 V; the box volume: 48 L; initial concentration of HCHO: 9.87 ppm). (d) Static efficiencies of MnO<sub>x</sub>/CNF and MnO<sub>x</sub>/CB<sub>0.2</sub>/CNF with electron injection and without electron injection. (e) Dynamic efficiency tests of CNF, MnO<sub>x</sub>, MnO<sub>x</sub>/CNF and MnO<sub>x</sub>/CB/CNF with different CB contents with electron injection and without electron injection (Temperature: ~25 °C; voltage: 10 V; the reaction tube volume: 40 mL; initial concentration of HCHO: 15 ppm; WHSV = 600000 mL/g<sub>MnO<sub>x</sub></sub>-h). (f) Histograms of HCHO removal and CO<sub>2</sub> production of MnO<sub>x</sub>/CNF and MnO<sub>x</sub>/CB<sub>0.2</sub>/CNF with electron injection and without electron injection. (g) Histograms of HCHO removal rate and HCHO conversion of MnO<sub>x</sub>/CNF and MnO<sub>x</sub>/CB<sub>0.2</sub>/CNF with electron injection and without electron injection. (h) Dynamic life test of MnO<sub>x</sub>/CNF and MnO<sub>x</sub>/CB<sub>0.2</sub>/CNF with electron injection and without electron injection. (i) Static cycle life diagram of MnO<sub>x</sub>/CB<sub>0.2</sub>/CNF with electron injection.

voltage for 24 h. It can be found that the temperature of the samples increases slightly with the increase of CB content. In particular, the increased temperature of MnO<sub>x</sub>/CB<sub>0.2</sub>/CNF is only less than 2 °C. The results indicate that the significant improvement in catalytic efficiency is not due to the increase of temperature.

Furthermore, for confirming that electrons can be injected into MnO<sub>x</sub> when MnO<sub>x</sub>/CB/CNF is energized, the I-V test was carried out for MnO<sub>x</sub> and MnO<sub>x</sub>/CB/CNF with different CB contents (Fig. 5d). The current in MnO<sub>x</sub> is 0.241 mA while that in MnO<sub>x</sub>/CB<sub>0.1</sub>/CNF is up to 0.426 mA, indicating that the current is not only passing through CB particles but also passing through MnO<sub>x</sub> during the catalysis with electron injection. As shown in the upper part of Fig. 5e, the electron injection influence of MnO<sub>x</sub>/CB<sub>0.2</sub>/CNF for HCHO catalytic oxidation was explored by real-time monitoring of the production of CO<sub>2</sub> under the action of the aerogel sample with and without electron injection. It was found that the CO<sub>2</sub> yield increases and reaches an extreme value during the electron injection process, and decreases when the aerogels are not energized, which changes periodically when the aerogels are energized and not energized. Comparatively, there was no significant change in CO<sub>2</sub>

production in the control sample with annular heated ceramic as a heat source, indicating that the increase in CO<sub>2</sub> production was not caused by a slight rise in temperature. Further, it is indicated that extra O\* is generated to participate in the catalytic reaction of HCHO during the electron injection process. Further, to prove that the catalyst could use the electrons supplied from the outside to promote the catalytic activity for HCHO oxidative degradation, the change of the current and CO<sub>2</sub> production under the action of MnO<sub>x</sub>/CB<sub>0.2</sub>/CNF was tested in the standard HCHO gas (HCHO: 15 ppm; O<sub>2</sub>: 21 vol%; N<sub>2</sub>) and pure N<sub>2</sub> respectively as shown in Fig. 5e. The current intensity on MnO<sub>x</sub>/CB<sub>0.2</sub>/CNF decreases under the flow of HCHO gas, meaning that some electrons are involved in the catalytic process of HCHO oxidation. In addition, XPS analysis revealed that the content of O<sub>A</sub> on the surface decreased after the sample was electrified, which could be attributed to the O<sub>2</sub> molecular adsorbed on the catalyst surface gains electrons provided by the outside and participating in the catalytic process. The current changes in the catalyst of MnO<sub>x</sub>/CB<sub>0.2</sub>/CNF aerogel under different mixed atmospheres are shown in Fig. 5f. The decrease in current means that O<sub>2</sub> is indeed involved in the acquisition of electrons from the outside during



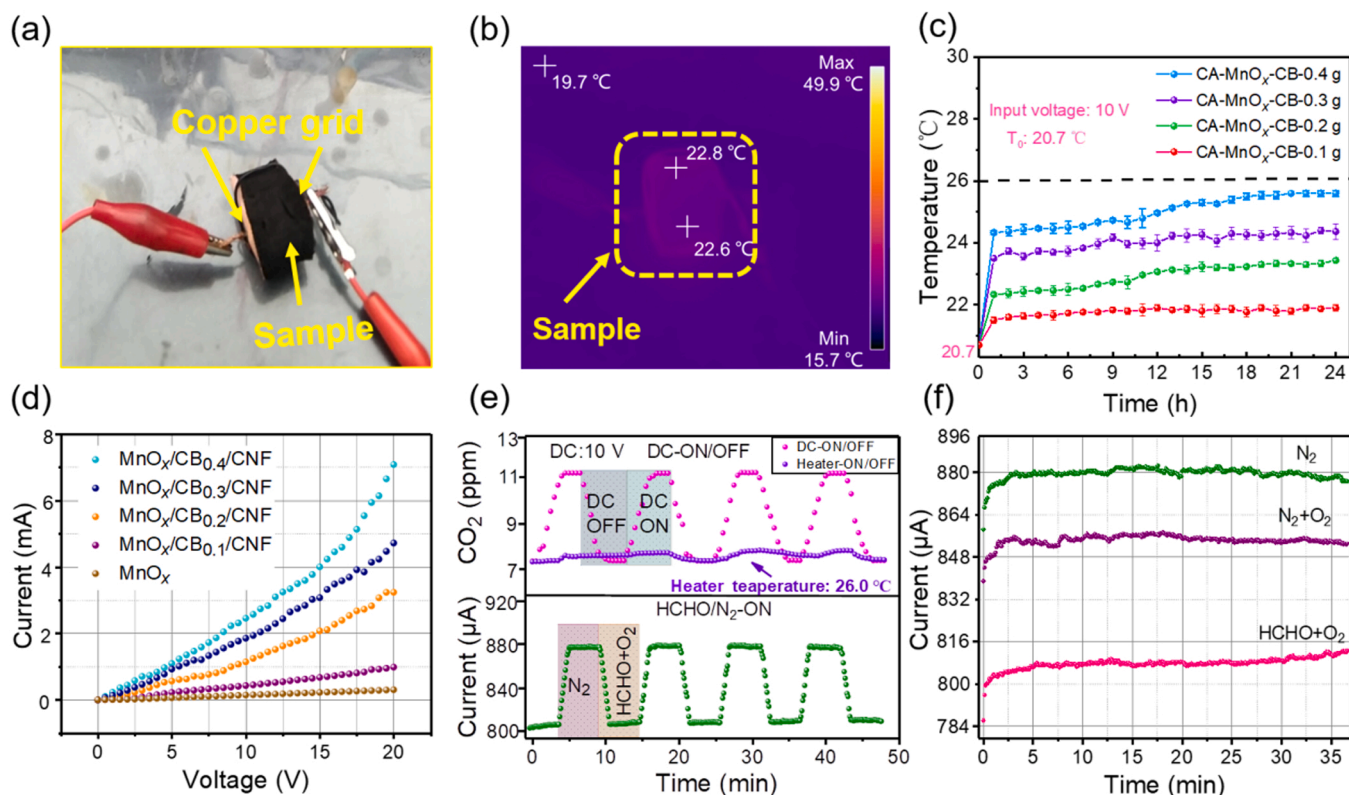


**Fig. 5.** (a) Temperature measuring device of electron injection. (b) The electron injection infrared temperature photograph. (c) Temperature variation of  $\text{MnO}_x/\text{CB}/\text{CNF}$  with different CB content within 24 h at 10 V voltage. (d) I-V curves of  $\text{MnO}_x$  and  $\text{MnO}_x/\text{CB}/\text{CNF}$  with different CB contents (the samples were pressed into  $1 \text{ cm} \times 1.1 \text{ cm}$  slices with a thickness of 0.1 mm for the I-V test). (e) The upper part shows the real-time  $\text{CO}_2$  production curve of  $\text{MnO}_x/\text{CB}_0.2/\text{CNF}$  with electron injection ON/OFF; the bottom part shows the real-time change curve of the current flowing into  $\text{HCHO}/\text{N}_2$  under the condition of sample  $\text{MnO}_x/\text{CB}_0.2/\text{CNF}$  electron injection. (f) The change curve of the current of  $\text{MnO}_x/\text{CB}_0.2/\text{CNF}$  into  $\text{HCHO}/\text{N}_2 + \text{O}_2/\text{N}_2$ . (The current voltage is 10 V DC, the temperature of the ceramic plate is set to 26 °C, and the gas flow rate is 2000 mL/min).

the electron injection process.

For further exploring the process of HCHO catalytic oxidation under the action of  $\text{MnO}_x/\text{CB}_0.2/\text{CNF}$  with and without electron injection, in-situ DRIFTS tests were performed to detect the changes in the functional groups of intermediates and final products during catalysis (Fig. 6a). The first 90 min is the spectrum of  $\text{MnO}_x/\text{CB}_0.2/\text{CNF}$  without electron injection exposed to  $\text{HCHO}/\text{O}_2$  at room temperature, the peaks of intermediate formate species ( $\text{HCOO}^-$ ,  $1426 \text{ cm}^{-1}$ ) gradually increased with the time prolongation of HCHO catalytic reaction [49], meaning the accumulation of intermediates is aggravated during the process of catalysis. At 90 min, the peak value of the characteristic peak corresponding to the intermediate reached the highest. At the moment, the electron injection of the catalyst was subsequently attempted to decompose the intermediate considering that the accumulation of it was the most critical factor for the deactivation of the catalyst at room temperature. After the sample was electrified persistently, the peak intensity of the intermediate gradually decreased, and the peaks corresponding to the final product of  $\text{H}_2\text{O}$  (the vibration peak of  $-\text{OH}$  located at  $900 \text{ cm}^{-1}$  [50] and carboxylic acid (the vibration peaks of  $\nu(\text{C}-\text{O})$  and  $\nu(\text{C}=\text{O})$  located at  $1236 \text{ cm}^{-1}$  and  $1713 \text{ cm}^{-1}$  respectively) [51] gradually increased with the extension of the electron injection time. Additionally, the peak intensity of the intermediate  $\text{HCOO}^-$  in the sample with electron injection is significantly smaller than that without electron injection by comparing the final spectra of the two samples (Fig. 6b). The results indicate that the electron injection had a significant effect on the removal of the intermediate and it was conducive to the regeneration of the catalyst.

It is well known that active oxygen species  $\text{O}^*$  (such as  $\text{O}^{2-}$ ,  $\text{O}^-$ ,  $-\text{OH}$  groups) play a critical role in HCHO catalytic degradation, the oxidation of HCHO and the further decomposition of intermediate products

depending on the participation of  $\text{O}^*$  species [21]. Therefore, compared with  $\text{MnO}_x/\text{CB}_0.2/\text{CNF}$  without electron injection, the excellent HCHO catalytic oxidation activity and long-term stability of the aerogel catalyst with electron injection are attributed to a large amount of  $\text{O}^*$  species generated during the catalysis. In order to demonstrate that electron injection could enhance the ability of aerogel catalysts to produce  $\text{O}^*$  active species, the EPR tests of superoxide radical ( $\text{O}_2^{\cdot-}$ ) were performed on  $\text{MnO}_x/\text{CB}_0.2/\text{CNF}$  that with and without electron injection (Fig. 6c). The results show that there are more  $\text{O}^*$  species ( $g = 2.004$ ) [24,52] generated in  $\text{MnO}_x/\text{CB}_0.2/\text{CNF}$  with electron injection than it without electron injection. Active species  $\text{O}^*$  produced on the surface of  $\text{MnO}_x$  mainly comes from electrons lost during the conversion of  $\text{Mn}^{3+}$  to  $\text{Mn}^{4+}$  captured by  $\text{O}_2$  adsorbed on the catalyst surface [53–55]. The EPR spectra with electron injection samples have a higher peak intensity compared with the not electron injection samples, indicating that the energized samples have a higher content of  $\text{O}^*$  on the surface. In addition, the  $\text{O}_2$ -TPD test (Fig. S7) showed that the number of surface reactive oxygen species and lattice oxygen mobility were improved in EI condition, which is consistent with the above analysis.

Based on the above analysis, we propose a mechanism of HCHO catalytic oxidative removal by a Mn-based aerogel catalyst with the assistance of persistent electron injection (Fig. 6d). The electrons from an external power source are injected into  $\text{MnO}_x$  in  $\text{MnO}_x/\text{CB}_0.2/\text{CNF}$  directly or by CB particles, and then a series of electron transfer processes occur in the catalyst  $\text{MnO}_x$ . On the one hand, the conversion from  $\text{Mn}^{4+}$  to  $\text{Mn}^{3+}$  in  $\text{MnO}_x$  is an electron gain process, which is accompanied by the formation of  $\text{O}_v$  and the escape of  $\text{O}_{\text{latt}}$ . The production of  $\text{O}_v$  could promote the adsorption of HCHO and  $\text{O}_2$  [28,56], and the escaped  $\text{O}_{\text{latt}}$  could be converted to  $\text{O}^*$  for the oxidation of HCHO and intermediate products [57,58]. On the other hand, the conversion from  $\text{Mn}^{3+}$  to

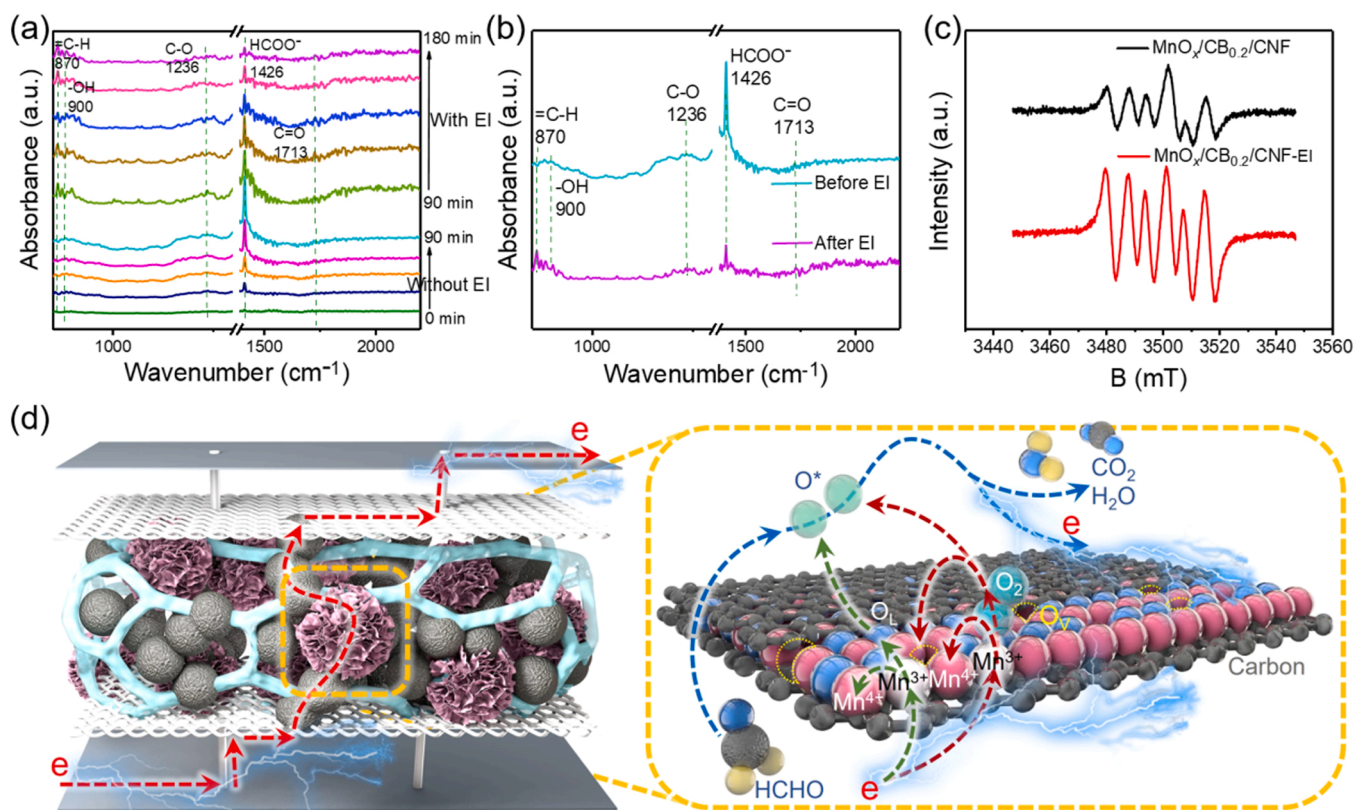


**Fig. 6.** (a) The in-situ DRIFTS of  $\text{MnO}_x/\text{CB}_{0.2}/\text{CNF}$  exposed to  $\text{HCHO}/\text{O}_2$  at room temperature: the samples without electron injection in 0–90 min and the sample with electron injection in 90–180 min (b) The in-situ DRIFTS of  $\text{MnO}_x/\text{CB}_{0.2}/\text{CNF}$  with electron injection and without electron injection were exposed to  $\text{HCHO}/\text{O}_2$  at room temperature for 90 min (c) The EPR spectrum of  $\text{MnO}_x/\text{CB}_{0.2}/\text{CNF}$  with electron injection and without electron injection at room temperature (energized voltage: 10 V, current: 0.1 A). (d) The mechanism diagram of  $\text{HCHO}$  catalytic oxidation when  $\text{MnO}_x/\text{CB}_{0.2}/\text{CNF}$  that with electron injection.

$\text{Mn}^{4+}$  in  $\text{MnO}_x$  is an electron loss process, and the lost electrons could promote the capture of  $\text{O}_2$  molecules. The trapped  $\text{O}_2$  molecules are activated as  $\text{O}^*$  species and  $\text{O}_{\text{latt}}$  on the surface of the catalyst, which is accompanied by  $\text{O}_{\text{latt}}$  filling in  $\text{O}_V$  to maintain the initial phase of  $\text{MnO}_x$  catalyst [59,60]. In particular, it can be seen that the migration of  $\text{O}_{\text{latt}}$  driven by electron transfer and the redistribution of electron density in  $\text{MnO}_x$  plays a crucial role in the whole catalytic process. In this case, electrons are injected into a catalyst and the electric field acts as an electron accelerator for the catalyst, promoting the migration of  $\text{O}_{\text{latt}}$  to improve the oxidation-reduction cycle capacity of the catalyst itself [26, 42], thus generating a large amount of  $\text{O}^*$  for the efficient oxidation and decomposition of  $\text{HCHO}$  molecules and intermediates [24,61,62]. Theoretically, as long as the electric field and oxygen supply are guaranteed,  $\text{O}^*$  species could be produced continuously in the process of catalytic oxidation. Consequently, the EICO strategy is expected to achieve long-term and effective catalytic oxidation by achieving the continuous production of  $\text{O}^*$  active species for the oxidative decomposition of  $\text{HCHO}$  molecules and intermediates.

#### 4. Conclusion

In this work, a three-dimensional conductive aerogel catalyst with cellulose nanofibers skeleton supported  $\text{MnO}_x$  nanoflowers was prepared by freeze-drying ( $\text{MnO}_x/\text{CB}/\text{CNF}$ ), which could realize the efficient and long-term  $\text{HCHO}$  degradation by introducing the electro-injection-enhanced catalytic oxidation strategy. In the dynamic  $\text{HCHO}$  removal test at the initial concentration of 15 ppm with the WHSV of 600000  $\text{mL}/\text{g}_{\text{MnO}_x}\cdot\text{h}$ , and the  $\text{HCHO}$ -to- $\text{CO}_2$  conversion efficiency of  $\text{MnO}_x/\text{CB}/\text{CNF}$  aerogel catalyst with electron injection reached to 76.27%, which is 26.4% higher than that of the catalyst without electron

injection. According to the electrical properties and surface substances characteristic of the catalyst, the significant improvement in catalytic degradation capacity is attributed to the accelerated transformation among  $\text{O}_2$ , lattice oxygen and reactive oxygen species  $\text{O}^*$  on the material surface under the action of EICO. What's more, the redistribution of and the rapid migration of electrons in the catalyst is enhanced under the action of electron injection to create more electron-rich regions as active sites for the conversion of  $\text{O}_2$  to reactive oxygen species, and then achieve efficient and long-term  $\text{HCHO}$  catalytic oxidation at room temperature. In addition, the high specific surface area ( $105.2 \text{ m}^2/\text{g}$ ) and porosity (88.68%) of aerogel catalyst further enhance the reciprocal flow and adsorption-desorption of gas molecules for achieving efficient and long-term  $\text{HCHO}$  catalytic oxidation at room temperature. This study innovatively proposed the catalytic oxidation behavior of  $\text{MnO}_x$  catalyst under the action of electron injection, and the prepared 3D aerogel can be directly used in practical applications, which is expected to solve the long-term catalytic problem of formaldehyde at room temperature, and provides a new idea for improving the catalytic efficiency and stability of other catalysts at room temperature.

#### Supporting Information

Supporting Information is available from the Wiley Online Library or from the author.

#### CRediT authorship contribution statement

**Chang Bao Han:** Ideas, Formulation or evolution of overarching research goals and aims, Project administration, Funding acquisition, **De Cai Fang:** Performing the experiments and Writing – original draft

preparation, **Jia Yu Zheng**: Conceptualization, Methodology, Visualization. **Wen Kang Zhao**: Writing – review & editing. **Yuan Gang Lu**: Methodology, Visualization. **Bei Chen Sun**: Software, Validation. **Ling Sun**: Supervision. **Xinxin Wang**: Methodology, Visualization. **Hui Yan**: Investigation.

## Declaration of Competing Interest

The authors declare that they have no known competing financial interests or personal relationships that could have appeared to influence the work reported in this paper.

## Data Availability

Data will be made available on request.

## Acknowledgement

The authors gratefully acknowledge the National Natural Science Foundation of China (NSFC, 52070006) and Beijing University Students Innovation and Entrepreneurship Training Inter School Cooperation Program (202298026).

## Appendix A. Supporting information

Supplementary data associated with this article can be found in the online version at [doi:10.1016/j.apcatb.2023.122837](https://doi.org/10.1016/j.apcatb.2023.122837).

## References

- [1] L. Miao, J. Wang, P. Zhang, Review on manganese dioxide for catalytic oxidation of airborne formaldehyde, *Appl. Surf. Sci.* 466 (2019) 441–453, <https://doi.org/10.1016/j.apsusc.2018.10.031>.
- [2] T. Salthammer, S. Mentese, R. Marutzky, Formaldehyde in the indoor environment, *Chem. Rev.* 110 (2010) 2536–2572, <https://doi.org/10.1021/cr800399g>.
- [3] V. Cammalleri, R.N. Pocino, D. Marotta, C. Protano, F. Sinibaldi, S. Simonazzi, M. Petyx, S. Iavicoli, M. Vitali, Occupational scenarios and exposure assessment to formaldehyde: a systematic review, *Indoor Air* 32 (2022), e12949, <https://doi.org/10.1111/ina.12949>.
- [4] J.P. Bellat, I. Bezverkhyy, G. Weber, S. Royer, R. Averlant, J.M. Giraudon, J. F. Lamonier, Capture of formaldehyde by adsorption on nanoporous materials, *J. Hazard. Mater.* 300 (2015) 711–717, <https://doi.org/10.1016/j.jhazmat.2015.07.078>.
- [5] Y. Shao, Y. Wang, R. Zhao, J. Chen, F. Zhang, R.J. Linhardt, W. Zhong, Biotechnology progress for removal of indoor gaseous formaldehyde, *Appl. Microbiol. Biotechnol.* 104 (2020) 3715–3727, <https://doi.org/10.1007/s00253-020-10514-1>.
- [6] Y. Wan, X. Fan, T. Zhu, Removal of low-concentration formaldehyde in air by DC corona discharge plasma, *Chem. Eng. J.* 171 (2011) 314–319, <https://doi.org/10.1016/j.cej.2011.04.011>.
- [7] A.H. Aissa, E. Puzenat, A. Plassais, J.M. Herrmann, C. Haehnel, C. Guillard, Characterization and photocatalytic performance in air of cementitious materials containing TiO<sub>2</sub>. Case study of formaldehyde removal, *Appl. Catal. B* 107 (2011) 1–8, <https://doi.org/10.1016/j.apcatb.2011.06.012>.
- [8] J. Guo, C. Lin, C. Jiang, P. Zhang, Review on noble metal-based catalysts for formaldehyde oxidation at room temperature, *Appl. Surf. Sci.* 475 (2019) 237–255, <https://doi.org/10.1016/j.apsusc.2018.12.238>.
- [9] C.C. Ou, C.H. Chen, T.S. Chan, C.S. Chen, S. Cheng, Influence of pretreatment on the catalytic performance of Ag/CeO<sub>2</sub> for formaldehyde removal at low temperature, *J. Catal.* 380 (2019) 43–54, <https://doi.org/10.1016/j.jcat.2019.09.028>.
- [10] K. Vikrant, K.H. Kim, F. Dong, D.W. Boukhvalov, W. Choi, Deep oxidation of gaseous formaldehyde at room-temperature by a durable catalyst formed through the controlled addition of potassium to platinum supported on waste eggshell, *Chem. Eng. J.* 428 (2022), 131177, <https://doi.org/10.1016/j.cej.2021.131177>.
- [11] B. Chen, X. Zhu, Y. Wang, L. Yu, C. Shi, Gold stabilized on various oxide supports catalyzing formaldehyde oxidation at room temperature, *Chin. J. Catal.* 37 (2016) 1729–1737, [https://doi.org/10.1016/S1872-2067\(16\)62470-1](https://doi.org/10.1016/S1872-2067(16)62470-1).
- [12] X. Liu, C. Wang, Y. Chen, Q. Qin, Y. Li, H. He, Formaldehyde oxidation on Pd/USY catalysts at room temperature: The effect of acid pretreatment on supports, *J. Environ. Sci.* 125 (2023) 811–822, <https://doi.org/10.1016/j.jes.2022.02.025>.
- [13] L. Shi, X. Zhou, Y. Guo, Y. Li, C. Yan, Q. Han, L. Zhang, W. Zhang, Designing of 3D MnO<sub>2</sub>-graphene catalyst on sponge for abatement temperature removal of formaldehyde, *J. Hazard. Mater.* 441 (2023), 129836, <https://doi.org/10.1016/j.jhazmat.2022.129836>.
- [14] C. Zhang, X. Qin, Z. Xue, X. Wang, Y. Shen, J. Zhu, Y. Wu, B. Meng, X. Meng, N. Yang, NaCl induced active hcp Co nanosheet for hydrogen production and formaldehyde abatement by formaldehyde steam reforming, *Chem. Eng. J.* 433 (2022), 134600, <https://doi.org/10.1016/j.cej.2022.134600>.
- [15] M.S. Niu, H.H. Yang, H. Zhou, X. Yi, X. Zhou, J. Zhan, Y. Liu, Synergy of the successive modification of cryptomelane MnO<sub>2</sub> by potassium insertion and nitrogen doping for catalytic formaldehyde oxidation, *Chem. Eng. J.* 431 (2022), 133928, <https://doi.org/10.1016/j.cej.2021.133928>.
- [16] T. Chang, Z. Shen, C. Ma, J. Lu, Y. Huang, S.K.P. Veerapandian, N. De Geyter, R. Morent, Process optimization of plasma-catalytic formaldehyde removal using MnO<sub>x</sub>-Fe<sub>2</sub>O<sub>3</sub> catalysts by response surface methodology, *J. Environ. Chem. Eng.* 9 (2021), 105773, <https://doi.org/10.1016/j.jece.2021.105773>.
- [17] H. Fang, C. Wang, D. Li, S. Zhou, Y. Du, H. Zhang, C. Hang, Y. Tian, T. Suga, Fabrication of Ag@Ag<sub>2</sub>O-MnO<sub>x</sub> composite nanowires for high-efficient room-temperature removal of formaldehyde, *J. Mater. Sci. Technol.* 91 (2021) 5–16, <https://doi.org/10.1016/j.jmst.2021.02.054>.
- [18] H. Zhao, J. Tang, Z. Li, J. Yang, H. Liu, L. Wang, Y. Cui, W. Zhan, Y. Guo, Y. Guo, Nickel oxide regulating surface oxygen to promote formaldehyde oxidation on manganese oxide catalysts, *Catal. Sci. Technol.* 11 (2021) 7110–7124, <https://doi.org/10.1039/d1cy01490k>.
- [19] J. Ji, X. Lu, C. Chen, M. He, H. Huang, Potassium-modulated δ-MnO<sub>2</sub> as robust catalysts for formaldehyde oxidation at room temperature, *Appl. Catal. B* 260 (2020), 118210, <https://doi.org/10.1016/j.apcatb.2019.118210>.
- [20] J. Li, P. Zhang, J. Wang, M. Wang, Birnessite-type manganese oxide on granular activated carbon for formaldehyde removal at room temperature, *J. Phys. Chem. C* 120 (2016) 24121–24129, <https://doi.org/10.1021/acs.jpcc.6b07217>.
- [21] R. Li, T. Huang, Y. Huang, M. Chen, Sc Lee, W. Ho, J. Cao, Unraveling the reaction mechanism of HCHO catalytic oxidation on pristine Co<sub>3</sub>O<sub>4</sub> (110) surface: a theoretical study, *Catalysts* 12 (2022), <https://doi.org/10.3390/catal12050560>.
- [22] M. Zhu, Y. Wen, L. Shi, Z. Tan, Y. Shen, K. Yin, L. Sun, Revealing the promoting effect of multiple Mn valences on the catalytic activity of CeO<sub>2</sub> nanorods toward soot oxidation, *Nanoscale* 14 (2022) 11963–11971, <https://doi.org/10.1039/d2nr03101a>.
- [23] M. Li, H. Zhang, Z. Liu, Y. Su, C. Du, Surface lattice oxygen mobility inspired peroxymonosulfate activation over Mn<sub>2</sub>O<sub>3</sub> exposing different crystal faces toward bisphenol A degradation, *Chem. Eng. J.* 450 (2022), 138147, <https://doi.org/10.1016/j.cej.2022.138147>.
- [24] N. Zou, Q. Nie, X. Zhang, G. Zhang, J. Wang, P. Zhang, Electrothermal regeneration by Joule heat effect on carbon cloth based MnO<sub>2</sub> catalyst for long-term formaldehyde removal, *Chem. Eng. J.* 357 (2019) 1–10, <https://doi.org/10.1016/j.cej.2018.09.117>.
- [25] W. Kang Zhao, J. Yu Zheng, C. Bao Han, J. Ruan, Y. Lu, K. Ling Zhou, T. Rui Zhai, H. Wang, H. Yan, MnO-PMMA self-powered triboelectric catalysts based on three-dimensional nanocomposite structures for formaldehyde degradation at room temperature, *Chem. Eng. J.* 440 (2022), 135877, <https://doi.org/10.1016/j.cej.2022.135877>.
- [26] X. Mei, X. Zhu, Y. Zhang, Z. Zhang, Z. Zhong, Y. Xin, J. Zhang, Decreasing the catalytic ignition temperature of diesel soot using electrified conductive oxide catalysts, *Nat. Catal.* 4 (2021) 1002–1011, <https://doi.org/10.1038/s41929-021-00702-1>.
- [27] D. Guo, S. Jiang, L. Jin, K. Huang, P. Lu, Y. Liu, CNT encapsulated MnO<sub>x</sub> for an enhanced flow-through electro-Fenton process: the involvement of Mn(IV), *J. Mater. Chem. A* 10 (2022) 15981–15989, <https://doi.org/10.1039/d2ta03445j>.
- [28] M. Wang, X. Hong, J. Chen, J. Li, X. Chen, J. Mi, Z. Liu, S. Xiong, Two-step hydrothermal synthesis of highly active MnO<sub>x</sub>-CeO<sub>2</sub> for complete oxidation of formaldehyde, *Chem. Eng. J.* 440 (2022), 135854, <https://doi.org/10.1016/j.cej.2022.135854>.
- [29] F. Lin, Z. Zhang, L. Xiang, L. Zhang, Z. Cheng, Z. Wang, B. Yan, G. Chen, Efficient degradation of multiple Cl-VOCs by catalytic ozonation over MnO catalysts with different supports, *Chem. Eng. J.* 435 (2022), 134807, <https://doi.org/10.1016/j.cej.2022.134807>.
- [30] Y. Luo, J. Wu, Y. Chen, J. Feng, L. Wang, L. Li, Y. Jiang, Y. Lei, J. Feng, A stabilization synthesis strategy for atomically dispersed metal-N<sub>4</sub> electrocatalysts via aerogel confinement and ammonia pyrolyzing, *Nano Energy* 104 (2022), 107869, <https://doi.org/10.1016/j.nanoen.2022.107869>.
- [31] R. Cao, L. Li, P. Zhang, Macroporous MnO<sub>2</sub>-based aerogel crosslinked with cellulose nanofibers for efficient ozone removal under humid condition, *J. Hazard. Mater.* 407 (2021), 124793, <https://doi.org/10.1016/j.jhazmat.2020.124793>.
- [32] X. Zhang, H. Guo, N. Xiao, X. Ma, C. Liu, L. Zhong, G. Xiao, Preparation and properties of epichlorohydrin-cross-linked chitosan/hydroxyethyl cellulose based CuO nanocomposite films, *Cellulose* 29 (2022) 4413–4426, <https://doi.org/10.1007/s10570-022-04511-y>.
- [33] H. Sehaqui, M. Salajkova, Q. Zhou, L.A. Berglund, Mechanical performance tailoring of tough ultra-high porosity foams prepared from cellulose I nanofiber suspensions, *Soft Matter* 6 (2010) 1824, <https://doi.org/10.1039/b927505c>.
- [34] C. He, Z. Jiang, M. Ma, X. Zhang, M. Douthwaite, J.W. Shi, Z. Hao, Understanding the promotional effect of Mn<sub>2</sub>O<sub>3</sub> on micro-/mesoporous hybrid silica nanocubic-supported Pt catalysts for the low-temperature destruction of methyl ethyl ketone: an experimental and theoretical study, *ACS Catal.* 8 (2018) 4213–4229, <https://doi.org/10.1021/acscatal.7b04461>.
- [35] J. Fu, P. Gao, L. Wang, Y. Zhang, Y. Deng, R. Huang, S. Zhao, Z. Yu, Y. Wei, G. Wang, S. Zhou, Regulating crystal facets of MnO<sub>2</sub> for enhancing peroxymonosulfate activation to degrade pollutants: performance and mechanism, *Catalysts* 12 (2022) 342, <https://doi.org/10.3390/catal12030342>.
- [36] J.Y. Zheng, W.K. Zhao, X. Wang, Z. Zheng, Y. Zhang, H. Wang, H. Yan, X. Song, C. B. Han, Electric-enhanced hydrothermal synthesis of manganese dioxide for the synergistic catalytic of indoor low-concentration formaldehyde at room



- temperature, *Chem. Eng. J.* 401 (2020), 125790, <https://doi.org/10.1016/j.cej.2020.125790>.
- [37] R. Yang, Y. Fan, R. Ye, Y. Tang, X. Cao, Z. Yin, Z. Zeng, MnO<sub>2</sub>-based materials for environmental applications, *Adv. Mater.* 33 (2021), 2004862, <https://doi.org/10.1002/adma.202004862>.
- [38] S. Wang, R. Yang, B. Li, R. Zhao, S. Yao, R. Liu, Z. Yang, Y.-M. Yan, Dual-directional electronic modulation of manganese oxides enabled by heterostructures for efficient sodium ion storage, *J. Power Sources* 521 (2022), 230969, <https://doi.org/10.1016/j.jpowsour.2021.230969>.
- [39] X. Guo, Z. Sun, H. Ge, Q. Zhao, T. Shang, Y. Tian, X.M. Song, MnO<sub>x</sub> bound on oxidized multi-walled carbon nanotubes as anode for lithium-ion batteries, *Chem. Eng. J.* 426 (2021), 131335, <https://doi.org/10.1016/j.cej.2021.131335>.
- [40] B. Zhang, J. Ji, B. Liu, D. Zhang, S. Liu, H. Huang, Highly efficient ozone decomposition against harsh environments over long-term stable amorphous MnO<sub>x</sub> catalysts, *Appl. Catal. B* 315 (2022), 121552, <https://doi.org/10.1016/j.apcatb.2022.121552>.
- [41] S. Zhang, W. Li, H. Tang, T. Huang, B. Xing, Revisit the adsorption of aromatic compounds on graphene oxide: roles of oxidized debris, *Chem. Eng. J.* 450 (2022), 137996, <https://doi.org/10.1016/j.cej.2022.137996>.
- [42] M. Torimoto, S. Ogo, D. Harjowinoto, T. Higo, J.G. Seo, S. Furukawa, Y. Sekine, Enhanced methane activation on diluted metal-metal ensembles under an electric field: breakthrough in alloy catalysis, *Chem. Commun.* 55 (2019) 6693–6695, <https://doi.org/10.1039/c9cc02794g>.
- [43] Y. Feng, C. Wang, C. Wang, H. Huang, H.C. Hsi, E. Duan, Y. Liu, G. Guo, H. Dai, J. Deng, Catalytic stability enhancement for pollutant removal via balancing lattice oxygen mobility and VOCs adsorption, *J. Hazard. Mater.* 424 (2022), 127337, <https://doi.org/10.1016/j.jhazmat.2021.127337>.
- [44] X. Tang, Y. Li, X. Huang, Y. Xu, H. Zhu, J. Wang, W. Shen, MnO<sub>x</sub>-CeO<sub>2</sub> mixed oxide catalysts for complete oxidation of formaldehyde: effect of preparation method and calcination temperature, *Appl. Catal. B* 62 (2006) 265–273, <https://doi.org/10.1016/j.apcatb.2005.08.004>.
- [45] X. Tang, J. Chen, Y. Li, Y. Li, Y. Xu, W. Shen, Complete oxidation of formaldehyde over Ag/MnO<sub>x</sub>-CeO<sub>2</sub> catalysts, *Chem. Eng. J.* 118 (2006) 119–125, <https://doi.org/10.1016/j.cej.2006.02.002>.
- [46] L. Li, S. Liu, M. Cheng, C. Lai, G. Zeng, L. Qin, X. Liu, B. Li, W. Zhang, Y. Yi, M. Zhang, Y. Fu, M. Li, M. Long, Improving the Fenton-like catalytic performance of MnO<sub>x</sub>-Fe<sub>3</sub>O<sub>4</sub>/biochar using reducing agents: a comparative study, *J. Hazard. Mater.* 406 (2021), 124333, <https://doi.org/10.1016/j.jhazmat.2020.124333>.
- [47] M. Shang, X. Zhang, J. Zhang, J. Sun, X. Zhao, S. Yu, X. Liu, B. Liu, X. Yi, Nitrogen-doped carbon composite derived from ZIF-8/polyaniline@cellulose-derived carbon aerogel for high-performance symmetric supercapacitors, *Carbohydr. Polym.* 262 (2021), 117966, <https://doi.org/10.1016/j.carbpol.2021.117966>.
- [48] Y. Chen, L. Zhang, Y. Yang, B. Pang, W. Xu, G. Duan, S. Jiang, K. Zhang, Recent progress on nanocellulose aerogels: preparation, modification, composite fabrication, applications, *Adv. Mater.* 33 (2021), 2005569, <https://doi.org/10.1002/adma.202005569>.
- [49] W. Liu, M. Shi, Y. Li, Z. Wu, L. Yang, S. Zhang, X. Xiao, C. Liu, W. Dai, C. Chen, X. Tu, J. Zou, X. Luo, Congregated-electrons-strengthened anchoring and mineralization of gaseous formaldehyde on a novel self-supporting Cu<sub>2-x</sub>Se/Cu<sub>2</sub>O heterojunction photocatalyst under visible lights: a viable mesh for designing air purifier, *Appl. Catal. B* 312 (2022), 121427, <https://doi.org/10.1016/j.apcatb.2022.121427>.
- [50] X. Li, Z. Jin, G. Bai, J. Wang, F. Gao, J. Linghu, Experimental study on the influence of water immersion on spontaneous combustion of anthracite with high concentrations of sulfur-bearing minerals, *J. Therm. Anal. Calorim.* 141 (2019) 893–903, <https://doi.org/10.1007/s10973-019-09073-z>.
- [51] Z. Wang, H. Yu, Y. Xiao, L. Guo, L. Zhang, X. Dong, Polydopamine mediated modification of manganese oxide on melamine sponge for photothermocatalysis of gaseous formaldehyde, *J. Hazard. Mater.* 407 (2021), 124795, <https://doi.org/10.1016/j.jhazmat.2020.124795>.
- [52] D. Chen, G. Zhang, M. Wang, N. Li, Q. Xu, H. Li, J. He, J. Lu, Pt/MnO<sub>2</sub> nanoflowers anchored to boron nitride aerogels for highly efficient enrichment and catalytic oxidation of formaldehyde at room temperature, *Angew. Chem. Int. Ed.* 60 (2021) 6377–6381, <https://doi.org/10.1002/anie.202013667>.
- [53] Y. Ma, G. Zhang, Sepiolite nanofiber-supported platinum nanoparticle catalysts toward the catalytic oxidation of formaldehyde at ambient temperature: efficient and stable performance and mechanism, *Chem. Eng. J.* 288 (2016) 70–78, <https://doi.org/10.1016/j.cej.2015.11.077>.
- [54] C. Mang, J. Luo, P. Cao, X. Zhang, M. Rao, G. Li, T. Jiang, Importance of water content in birnessite-type MnO<sub>2</sub> catalysts for HCHO oxidation: mechanistic details and DFT analysis, *Chemosphere* 287 (2022), 132293, <https://doi.org/10.1016/j.chemosphere.2021.132293>.
- [55] G. Li, M. Chen, X. Huang, P. Wang, Manganese-doped cobalt tetroxide for formaldehyde oxidation, *J. Environ. Chem. Eng.* 10 (2022), 108328, <https://doi.org/10.1016/j.jece.2022.108328>.
- [56] Y. Huang, Y. Liu, W. Wang, M. Chen, H. Li, S.-c Lee, W. Ho, T. Huang, J. Cao, Oxygen vacancy-engineered  $\delta$ -MnO<sub>x</sub>/activated carbon for room-temperature catalytic oxidation of formaldehyde, *Appl. Catal. B* 278 (2020), 119294, <https://doi.org/10.1016/j.apcatb.2020.119294>.
- [57] A. Yusuf, Y. Sun, C. Snape, J. He, C. Wang, Y. Ren, H. Jia, Low-temperature formaldehyde oxidation over manganese oxide catalysts: potassium mediated lattice oxygen mobility, *Mol. Catal.* 497 (2020), 111204, <https://doi.org/10.1016/j.mcat.2020.111204>.
- [58] J. Chen, H. Tang, M. Huang, Y. Yan, J. Zhang, H. Liu, J. Zhang, G. Wang, R. Wang, Surface lattice oxygen activation by nitrogen-doped manganese dioxide as an effective and longevous catalyst for indoor HCHO decomposition, *ACS Appl. Mater. Interfaces* 13 (2021) 26960–26970, <https://doi.org/10.1021/acsami.1c04369>.
- [59] X. Zhao, D. Xu, Y. Wang, Z. Zheng, K. Li, Y. Zhang, R. Zhan, H. Lin, Electric field assisted benzene oxidation over Pt-Ce-Zr nano-catalysts at low temperature, *J. Hazard. Mater.* 407 (2021), 124349, <https://doi.org/10.1016/j.jhazmat.2020.124349>.
- [60] H. Huang, X. Ye, H. Huang, L. Zhang, D.Y.C. Leung, Mechanistic study on formaldehyde removal over Pd/TiO<sub>2</sub> catalysts: oxygen transfer and role of water vapor, *Chem. Eng. J.* 230 (2013) 73–79, <https://doi.org/10.1016/j.cej.2013.06.035>.
- [61] K. Wang, Y. Zeng, W. Lin, X. Yang, Y. Cao, H. Wang, F. Peng, H. Yu, Energy-efficient catalytic removal of formaldehyde enabled by precisely Joule-heated Ag/Co<sub>3</sub>O<sub>4</sub>/mesoporous-carbon monoliths, *Carbon* 167 (2020) 709–717, <https://doi.org/10.1016/j.carbon.2020.06.055>.
- [62] K. Li, K. Liu, H. Ni, B. Guan, R. Zhan, Z. Huang, H. Lin, Electric field promoted ultra-lean methane oxidation over Pd-Ce-Zr catalysts at low temperature, *Mol. Catal.* 459 (2018) 78–88, <https://doi.org/10.1016/j.mcat.2018.08.021>.